

Banner appropriate to article type will appear here in typeset article

1 **Influence of Electric Potential Decay to the Impact 2 Regimes of Droplets on a Hydrophobic Electrode**

3 **Ziqiang Ma¹, and Xinping Zhou^{1,2†}**

4 ¹School of Mechanical Science and Engineering, Huazhong University of Science and Technology, Wuhan
5 430074, PR China

6 ²State Key Laboratory of Intelligent Manufacturing Equipment and Technology, Huazhong University of
7 Science and Technology, Wuhan 430074, China

8 (Received xx; revised xx; accepted xx)

9 Direct numerical simulations of Popinet (2003)

10 **Key words:** Authors should not enter keywords on the manuscript, as these must be chosen by
11 the author during the online submission process and will then be added during the typesetting
12 process (see [Keyword PDF](#) for the full list). Other classifications will be added at the same
13 time.

14 **1. Introduction**

15 In dielectrowetting research, the effect of non-uniform electric fields on liquid wetting has
16 been established. McHale *et al.* (2011), for instance, demonstrated that tailored non-uniform
17 fields enable control of the contact angle and wetting state.

18 The dynamics of droplet impact on solid surfaces is a classical problem in fluid mechanics,
19 with various engineering applications, including inkjet printing, spray cooling, and microfluidic
20 actuation. The interaction between inertia, surface tension, viscosity, and wettability
21 gives rise to complex behaviors, such as spreading, retraction, rebound, or splashing. In
22 recent years, the ability to actively modulate wettability through external stimuli has attracted
23 significant interest, particularly via electrowetting-on-dielectric (EWOD). In EWOD systems,
24 the apparent contact angle of a droplet can be dynamically controlled by applying an electric
25 potential across a dielectric-coated electrode, enabling real-time tuning of droplet behavior.

26 Previous studies have extensively investigated the role of electrowetting in modifying
27 contact angle hysteresis, controlling spreading dynamics, and suppressing rebound. Most of
28 these works, however, assume that the applied electric field is spatially uniform. In practical
29 implementations—especially when thin electrodes with finite conductivity or localized voltage
30 sources are employed—the electric potential may decay laterally along the substrate. This non-
31 uniformity can lead to spatial gradients in wettability and contact angle, potentially altering
32 the droplet impact regimes. Despite its physical relevance, the influence of electric potential
33 decay on droplet dynamics has received little attention and remains poorly understood.

† Email address for correspondence: JFMEditorial@cambridge.org

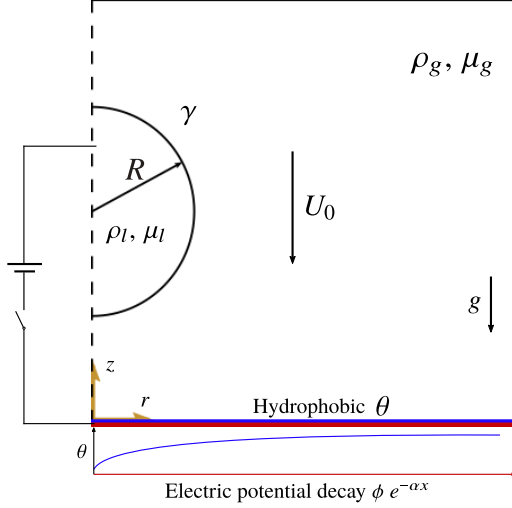


Figure 1: Schematic of the physical model and governing parameters. A liquid droplet of radius R , density ρ_l and viscosity μ_l impacts a hydrophobic substrate with initial velocity U_0 under gravity g . The surrounding gas has density ρ_g and viscosity μ_g . The liquid-gas interface is characterized by surface tension γ . The substrate is subject to electrowetting, with the apparent contact angle θ modified by an electric potential that decays along the substrate as $\phi e^{-\alpha x}$. The coordinate system is defined by the radial direction r and vertical direction z .

In this work, we study the impact of a millimetric water droplet on a hydrophobic substrate subject to a laterally decaying electric potential of the form $\phi(r) = \phi_0 e^{-\alpha r}$, where α is the electric potential decay constant. Using a dimensionless formulation, we investigate how this spatial variation in potential affects the contact angle distribution, impact-induced deformation, and rebound behavior. Furthermore, we extend our analysis to include time-harmonic potentials to examine the frequency-dependent response of the droplet under alternating fields. A combination of numerical simulation and phase-space classification is employed to delineate different behavioral regimes.

The paper is organized as follows. Section 2 introduces the problem formulation and numerical methods. Section 3 presents a phase diagram and classification of electrowetting-induced wettability. The influence of electric potential decay on droplet dynamics is then examined, followed by an analysis of the frequency-dependent response of droplet behavior under time-varying electric potentials. Conclusions are drawn in Section 4.

2. Problem and method

2.1. Governing equations and numerics models

Consider a water droplet of diameter D placed upon the substrate exhibiting electric potential decay $\phi_0 e^{-\alpha r}$, where α is the electric potential decay constant. The droplet impacts the electrowetting surface with the velocity U_0 . The density and viscosity are denoted by ρ and μ , with subscripts l and g indicating the liquid and the surrounding gas. In the electrowetting on dielectric (EWOD) phenomena under consideration, the wettability of substrate is varied by applied electric current. The variation of contact angle which is induced by electrowetting can be described by the Young-Lippmann equation

56 $\cos(\theta_{ew}) = \cos \theta_s + \frac{\epsilon_0 \epsilon_r}{2\gamma d} \phi^2.$ (2.1)

57 θ_s is the static contact angle, θ_{ew} is the electrowetting induced contact angle, and γ is
 58 the surface tension. ϵ_0 is the vacuum's permittivity, ϵ_r and d is the dielectric constant and
 59 dielectric thickness. Due to the electric potential decay, the contact angle at the wall exhibits a
 60 trend of being lower at the center and higher at the periphery. Figure 1 shows the configuration
 61 of the water droplet in the domain for computations.

62 The water droplet and surrounding fluid are controlled by the continuity and momentum
 63 equations for the incompressible fluids

64 $\nabla \cdot \mathbf{u} = 0,$ (2.2)

65 $\rho(\partial_t \mathbf{u} + \mathbf{u} \nabla \cdot \mathbf{u}) = -\nabla p + \nabla \cdot \mu(\nabla \mathbf{u} + \nabla^T \mathbf{u}) + \gamma \kappa \delta_s \mathbf{n} + \rho \mathbf{g},$ (2.3)

66 where p is the pressure, \mathbf{g} is the gravity acceleration. A volume fraction function, denoted by
 67 c , is introduced to distinguish between the two immiscible fluid phases in the computational
 68 domain. Specifically, $c = 1$ corresponds to the liquid phase (water), and $c = 0$ corresponds to
 69 the gas phase (air). This function is constructed based on the known location of the interface.
 70 Since the density ρ and viscosity μ are constant within each phase, their spatial distributions
 71 across the domain can be conveniently expressed in terms of c as follows:

72 $\rho = \rho_g + (\rho_l - \rho_g)c,$
 $\mu = \mu_g + (\mu_l - \mu_g)c,$ (2.4)

73 where subscripts l and g denote the liquid and gas phases, respectively. The function c
 74 thus implicitly tracks the interface and evolves in time according to the following advection
 75 equation:

76 $\partial_t c + \nabla \cdot (c \mathbf{u}) = 0,$ (2.5)

77 We nondimensionalize all variables using the diameter of the drop D . Therefore, the timescale
 78 is $\tau = \sqrt{\rho_l D^3 / \gamma}$, the velocity scale is $\sqrt{\gamma / \rho_l D}$, and the length scale is D . The three
 79 nondimensional parameters, the Ohnesorge number, the Weber number, the Bond number:

80 $Oh = \frac{\mu}{\sqrt{\rho \gamma D}}, We = \frac{\rho D U_0}{\gamma}, Bo = \frac{\rho g D^2}{\gamma}.$ (2.6)

81 We consider the effect of gravity by setting Bo as a constant in all cases. And all the material
 82 properties the density ratio ρ_g / ρ_l , the viscosity ratio μ_g / μ_l are typically defined as constants
 83 1×10^{-3} and 1.79×10^{-2} . Here, a Volume-of-Fluid (VOF) method of combining an adaptive
 84 quad spatial discretisation (Popinet 2003, 2009; Afkhami *et al.* 2009, 2018) is chosen to
 85 implement the electrowetting technique with dynamic contact angle model.

86 When a sessile droplet equilibrium on the substrate, the static contact angle θ_s is the angle
 87 between the interface of droplet and the substrate surface. The dynamic contact angle θ_D is
 88 implemented using the molecular kinetic theory (MKT) (Duvivier *et al.* 2013; Cheng *et al.*
 89 2018; Kumar & Pathak 2024). Using the theory, the dynamic contact angle θ_D and contact
 90 line velocity v_{cl} have the following relationship:

91 $v_{cl} = 2k_s^0 l \left(\frac{h}{\mu V_m} \right) \sinh \left[\frac{\gamma}{2nk_B T} (\cos \theta_s - \cos \theta_D) \right].$ (2.7)

Parameter	Description	Value
ϵ_0	Vacuum permittivity	8.85×10^{-12} m
ϵ_r	Dielectric constant	2.6
k_s^0	Dielectric constant	4.5627×10^{10} s ⁻¹
l	Molecular displacement	5×10^{-10} m
h	Planck constant	6.63×10^{-34} Js
V_m	Molecular volume	3×10^{-29} m ³
k_B	Boltzmann constant	1.38×10^{-23} m ³
T	Temperature	298.15 K
d	Dielectric thickness	1×10^{-5} m

Table 1: Summary of operating parameters used for MKT model in the simulations.

The values of all reference parameters employed in the present study are summarized in Table 1. The contact line velocity is limited by the maximum for the dynamic contact angle of 180° and the minimum for the dynamic contact angle of 0°:

$$v_{\text{cl}180^\circ} = 2k_s^0 l \left(\frac{h}{\mu V_m} \right) \sinh \left[\frac{\gamma}{2n k_B T} (\cos \theta_s + 1) \right], \quad (2.8)$$

$$-v_{\text{cl}0^\circ} = 2k_s^0 l \left(\frac{h}{\mu V_m} \right) \sinh \left[\frac{\gamma}{2n k_B T} (1 - \cos \theta_s) \right]. \quad (2.9)$$

Although the contact line velocity v_{cl} , can theoretically exceed both upper and lower limit, the numerical simulations are constrained to operate within the limits specified by Eqs. 2.8 and 2.9. Under reference conditions, the dynamic contact angle (DCA) is inferred from the prescribed contact line velocity by inverting the corresponding relation. The expression used to compute the DCA is given by

$$\theta_D = \cos^{-1} \left[\cos \theta_s - \left(\frac{2n k_B T}{\gamma} \sinh^{-1} \left(\frac{v_{\text{cl}} \mu V_m}{2k_s^0 l h} \right) \right) \right]. \quad (2.10)$$

Electrowetting technique enables dynamic control of surface wettability by applying an electric potential across a conductive droplet. When the electric potential is established between the droplet and an underlying electrode, charges accumulate at the three-phase contact line. This localized buildup of electric charge leads to a reduction in the interfacial energy between the droplet and the substrate. The extent of contact angle modulation depends on the properties of the liquid, the characteristics of the substrate, and the parameters of the applied electric field in Eqs. 2.1. Accordingly, the relationship between the dynamic contact angle induced by electrowetting and contact line velocity is described by:

$$\theta_{\text{ED}} = \cos^{-1} \left[\cos \theta_s + \frac{\epsilon_0 \epsilon_r}{2\gamma d} \phi^2 - \left(\frac{2n k_B T}{\gamma} \sinh^{-1} \left(\frac{v_{\text{cl}} \mu V_m}{2k_s^0 l h} \right) \right) \right]. \quad (2.11)$$

2.2. Problem setup and numerics validation

As shown in figure 1, a spherical water droplet of diameter D is initially positioned in close proximity to the lower boundary, which consists of a solid substrate subject to an applied electric potential. The droplet impacts the surface with a prescribed velocity U_0 , and the dynamics are governed by the electrowetting-on-dielectric (EWOD) mechanism. Initially,

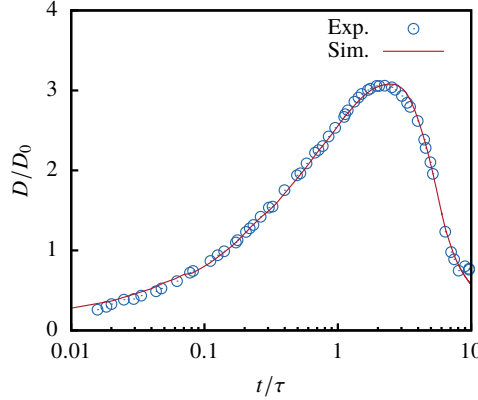


Figure 2: Comparison of drop spreading radius during impact process obtained from experiment data reported by Šikalo *et al.* (2002).

117 the contact angle is static, with $\theta_s = 90^\circ$. Upon actuation, the contact angle varies dynamically
 118 in response to the applied voltage, which is both spatially and temporally dependent. The
 119 applied voltage is defined as

$$120 \quad \phi(r, t) = \phi_0 \cos(2\pi f t) \cdot e^{-\alpha r}, \quad (2.12)$$

121 where ϕ_0 is the peak amplitude of electric potential, f is the oscillation frequency, and
 122 α characterizes the radial decay of the electric potential, accounting for the influence of a
 123 uniform resistance on the potential distribution along the dielectric layer. The computational
 124 domain is taken as $10D \times 10D$ to ensure sufficient space for droplet deformation and spreading
 125 during impact and subsequent evolution. The bottom of the computational domain ($z = 0$)
 126 is a no-slip boundary condition, and the left ($r = 0$) is an axisymmetric boundary condition.
 127 All remaining boundaries of the computational domain are open boundary conditions.

128 Building upon earlier incompressible flow theories (Smith *et al.* 2003; Korobkin *et al.*
 129 2008), Mandre *et al.* (2009) derived a criterion to assess the relevance of gas compressibility
 130 during high-velocity droplet impacts. Specifically, they introduced a non-dimensional com-
 131 pressibility parameter defined as the ratio between the ambient atmospheric pressure and a
 132 characteristic lubrication pressure in the gas layer:

$$133 \quad \epsilon = \frac{P_{\text{atm}}}{\left(0.5 * DU_0^7 \rho_l^4 / \mu_g\right)^{1/3}}, \quad (2.13)$$

134 where P_{atm} is the ambient atmospheric pressure, and μ_g the gas viscosity. According to their
 135 analysis, gas compressibility becomes significant when $\epsilon^{-1} \gtrsim 3$. In light of this criterion,
 136 and supported by the conclusions of Li & Thoroddsen (2015) and Mandre *et al.* (2009), we
 137 neglect gas compressibility effects in the present study. The estimated range of the inverse
 138 compressibility parameter in our simulations is $\epsilon^{-1} \approx 0.1\text{--}2.0$, which remains well below
 139 the threshold for compressibility to play an important role. These values differ slightly from
 140 those in earlier studies due to variations in Ohnesorge (Oh) and Weber (We) numbers, but
 141 they still justify the assumption of incompressibility for the gas phase under the current
 142 impact conditions.

143 To ensure the accuracy and reliability of the numerical model, simulation results are
 144 validated against experimental data reported by Šikalo *et al.* (2002). Figure 2 presents the time

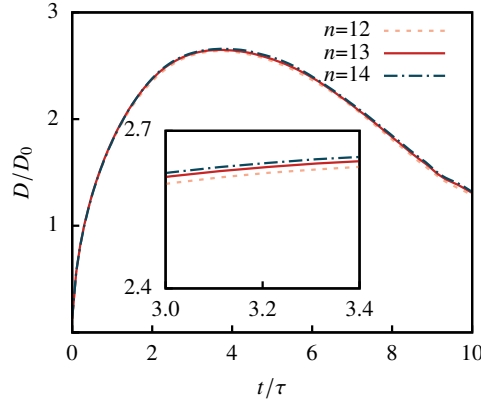


Figure 3: Verification of grid independence for the droplet spreading radius during impact, based on simulations performed at $We = 20$.

145 evolution of the spreading radius of the droplet, normalized by its initial radius, as a function
 146 of the non-dimensional time. All physical parameters used in the simulation are consistent
 147 with those in the referenced experiment. In particular, the Weber number is $We = 44$, and the
 148 static contact angle is set to 100° , matching the experimental configuration. The simulation
 149 results exhibit excellent agreement with the experimental data, thereby demonstrating the
 150 validity of the computational model in capturing the essential physics of droplet impact and
 151 spreading dynamics.

152 For grid independence, we compare the spreading radius with time obtained from
 153 simulations, using different grid resolutions to assess the effect of varying grid sizes
 154 on the simulation accuracy. Figure 3 shows the finest grid sizes from low to high are
 155 $\Delta/D = 4.8 \times 10^{-3}$, $\Delta/D = 2.4 \times 10^{-3}$, and $\Delta/D = 1.2 \times 10^{-3}$ for the given computational
 156 domain. The orange dash line is the finest grid level 12, the red line is the finest grid level 13
 157 and the blue dash line is the finest grid 14. Despite these minor differences in the three levels,
 158 we notice that the middle grid size level reach the results are not significantly influenced by
 159 the grid resolution, while also accounting for the prohibitive computational costs involved.
 160 Thus, we choose the middle grid size level for all of our simulations.

161 3. Results

162 In order to compare the dynamics of droplet motion, we first deployed droplets to impact on
 163 substrates with the same initial static contact angle, $\theta_s = 90^\circ$. The motion of the droplets
 164 can be divided into three stages: spreading, retracting, and rebounding, after which they
 165 detach from the substrate. To actively control the contact angle during these dynamics, a
 166 voltage is applied between the conducting droplet and an underlying insulated electrode.
 167 This configuration, typical of the electrowetting-on-dielectric (EWOD) setup, consists of
 168 a hydrophobic dielectric layer that electrically isolates the droplet from the conductive
 169 substrate. When the electric field is activated, charges accumulate on the droplet side of the
 170 dielectric layer, forming a capacitor-like structure. This localized charge distribution results
 171 in a reduction of the interfacial energy near the contact line, thereby decreasing the apparent
 172 contact angle θ_{ED} of the droplet. The variation of the contact angle θ_{ED} with applied voltage
 173 is governed by the Young-Lippmann equation. To investigate the role of electric potential
 174 decay in electrowetting-induced wettability changes, we conduct droplet impact experiments
 175 at fixed dimensionless parameters, $Oh = 2.621 \times 10^{-3}$ and $Bo = 0.536$.

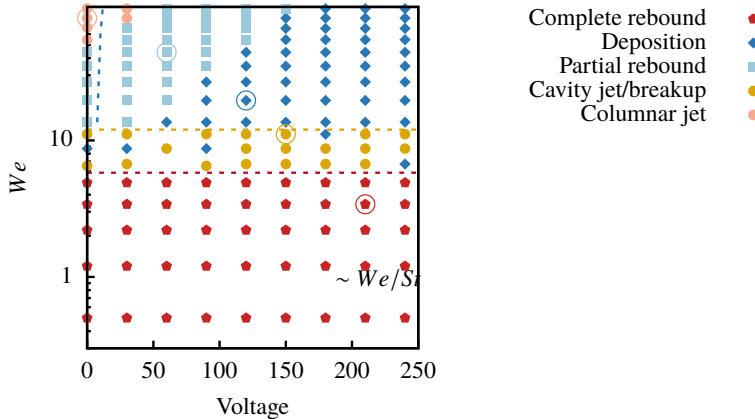


Figure 4: Phase diagrams of the motion state of a droplet impacting with the applied voltage varies obtained from simulations. Open-circle markers denote the selected cases corresponding to each regime.

3.1. Phase Diagram and Classification of Electrowetting-Induced Wettability

When droplet impact the substrate with different electrowetting-induced wettability, it exhibits distinct dynamic reaction owing to voltage-induced variations in the equilibrium contact angle. Since the contact angle governs the balance of interfacial forces, the difference in wettability significantly influences the spreading, retraction, and rebound behaviour of the droplet. On a substrate with an equilibrium contact angle of 90° , the droplet follows the classical sequence of spreading, receding, and rebounding. At low impact velocities (i.e., low Weber numbers), the droplet may remain entirely separated from the substrate by a thin air layer, resulting in non-contact bouncing. At sufficiently high Weber numbers, the droplet undergoes splashing, with the emission of secondary droplets. To systematically characterise the influence of electrowetting, we construct a phase diagram in the applied voltage-Weber number plane that delineates the regimes of droplet impact behaviour under varying wettability conditions. Figure 4 delineates the behavioural phase diagram of droplet impact regimes across applied voltages and Weber numbers, encompassing low-velocity complete rebound and cavity-induced jetting, alongside moderate-to-high-velocity partial rebound, deposition, and columnar liquid jetting regimes.

Figure 5 presents a morphological chronology of droplet evolution across distinct regimes, capturing the complete progression from initial contact to final configuration. Sequentially arranged are: columnar jetting, partial rebound, deposition, cavity-induced breakup, and complete rebound – corresponding to the cases of the phase diagram's open-circle markers. Key features include central jet ejection (columnar jetting), necking phenomena (partial rebound), and filamentous jets (cavity regime/breakup), while deposition and complete rebound are distinguished by their final equilibrium states.

When a droplet impacts a solid wall at relatively high velocity, it typically exhibits splashing. For low-viscosity droplets, however, splashing behaviour is normally suppressed (Jian *et al.* 2018). Upon contacting the substrate, the droplet's kinetic energy is rapidly converted into surface energy, driving the spreading until the maximum radius is reached. Subsequently, under the influence of significant surface energy potential, the droplet retracts rapidly. The radially inward convergence of capillary waves from the spreading periphery focuses at the axisymmetric centre, resulting in the formation of a vertical columnar jet. Figure 6 shows the droplet impacting sequence, tracing the droplet from spreading through

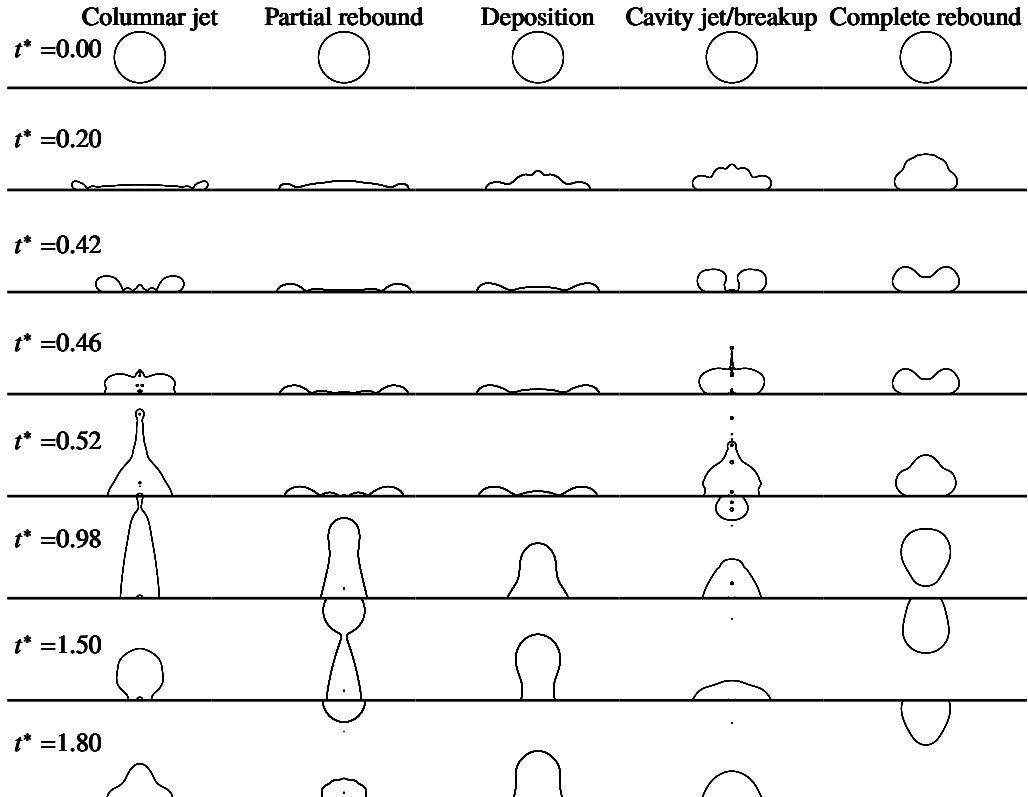


Figure 5: Phase diagrams of the motion state of a droplet impacting with the applied voltage varies obtained from simulations.

retraction to capillary wave focusing and vertical liquid jet formation. Conversely, at low Weber numbers, the cavity-jet/breakup regime is observed. In this regime, the air film beneath the droplet remains intact throughout the spreading process. And the convergence of slowly propagating capillary waves during spreading forms a central cavity. Subsequent accelerated retraction causes cavity collapse, inducing high-velocity jet ejection. This process typically results in prompt and extensive fragmentation due to vapour cavity implosion. Figure 7 illustrates the complete evolution of central cavity formation through collapse-induced jetting. The implosion-driven jets exhibit elevated pressures, resulting in ejected microdroplets with enhanced velocities and reduced diameters.

Within the moderate impact velocity regime, droplets typically achieve extensive spreading radii. Owing to substantial surface energy storage, accelerated retraction imparts sufficient kinetic energy to induce necking phenomena, ultimately enabling rebound detachment (partial rebound). In contrast, during deposition events, droplets possess insufficient kinetic energy upon impact. Significant viscous dissipation during spreading depletes momentum reserves, precluding rebound. Consequently, residual energy is exhausted through damped capillary-inertial oscillations until complete immobilisation (deposition).

To elucidate the energy evolution across the two regimes, we consider the total energy of the droplet and substrate system. The relevant energetic contributions are the kinetic energy E_k , the interfacial (capillary) energy E_γ , the electrostatic energy stored in the dielectric E_e , the gravitational potential E_g (which may be negligible in the small-Bond-number limit),

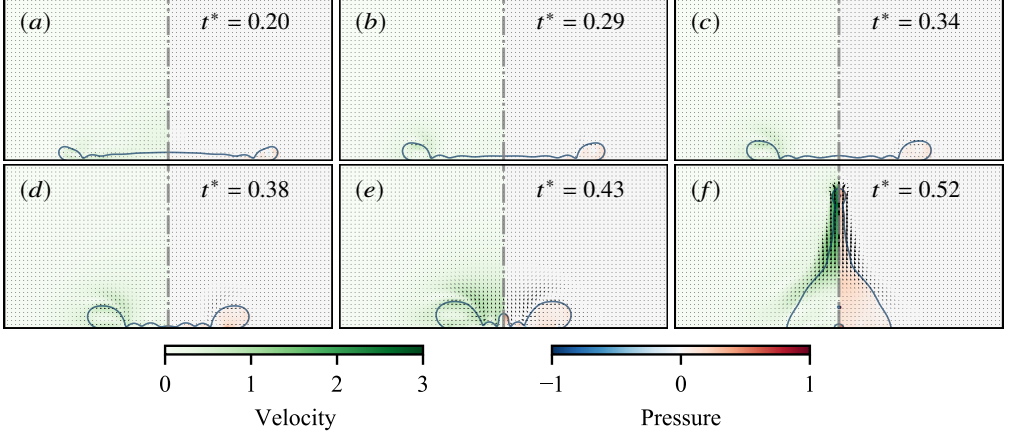


Figure 6: The formation process of columnar jet droplets. The left snapshots show the magnitude of the velocity field normalized by the initial impact velocity, and the right snapshots show the dimensionless pressure. The black arrow is the velocity vector of flow. The blue line represents the interface between the droplet and the surrounding gas.

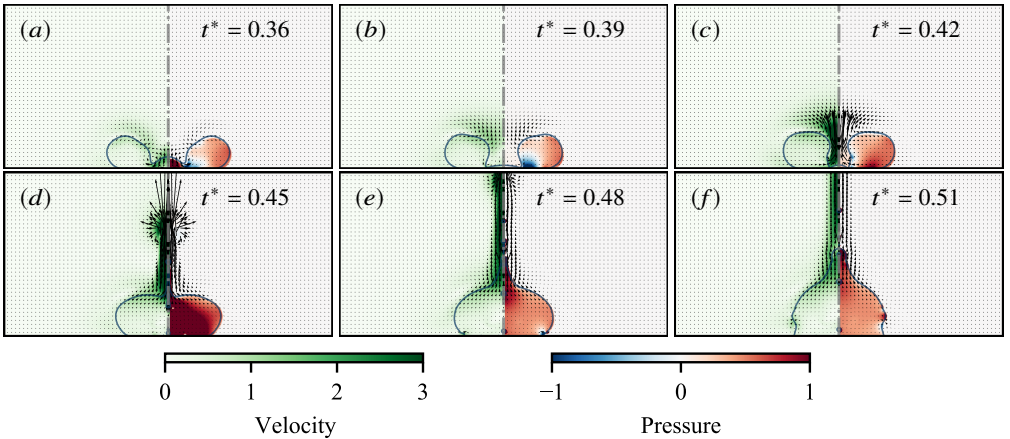


Figure 7: The formation process of cavity jet/breakup droplets. The left snapshots show the magnitude of the velocity field normalized by the initial impact velocity, and the right snapshots show the dimensionless pressure. The black arrow is the velocity vector of flow. The blue line represents the interface between the droplet and the surrounding gas.

227 and the viscous dissipation E_d . The integrated energy balance between an initial time 0 and
228 time t reads

$$229 \quad \Delta(E_k + E_g + E_\gamma + E_e) = -E_d + W_{\text{ext}}. \quad (3.1)$$

230 where W_{ext} denotes any external mechanical work (zero in the absence of external forcing).
231 The electrostatic energy stored in the dielectric under the contact patch (parallel-plate
232 approximation) is

$$233 \quad E_e(t) = \frac{1}{2}C(t)\phi^2 = \frac{1}{2}\frac{\epsilon_0\epsilon_r A_{\text{SL}}(t)}{d}\phi^2, \quad (3.2)$$

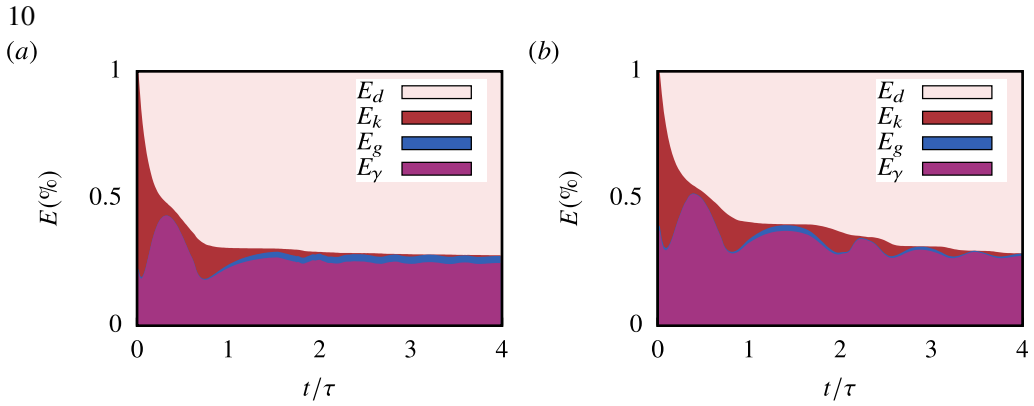


Figure 8: The energy transformations during the formation of (a) partial rebound, (b) deposition in the process of droplet impact on the substrate. The horizontal axis represents dimensionless time, and the vertical axis represents the distribution of the three energies.

where ϕ denotes the applied potential (constant-voltage case), d the dielectric thickness, and $A_{\text{SL}}(t)$ the instantaneous solid-liquid contact area.

It is often convenient to express the interfacial energy using Young's relation. Taking $\gamma_{\text{SG}}A_{\text{S}}$ as an arbitrary reference (constant) contribution and using $\gamma_{\text{LG}} \cos \theta_s = \gamma_{\text{SG}} - \gamma_{\text{SL}}$, the change in capillary energy relative to the reference can be written

$$\Delta E_\gamma = \gamma_{\text{LG}}(A_{\text{LG}} - A_{\text{SL}} \cos \theta_s). \quad (3.3)$$

Under electrowetting 2.1 limit, if we compute the capillary energy using the voltage-dependent contact angle θ_{ew} ,

$$E_\gamma^{(\text{ew})} = \gamma_{\text{LG}}(A_{\text{LG}} - A_{\text{SL}} \cos \theta_{\text{ew}}), \quad (3.4)$$

then substituting (2.1) yields the identity

$$E_\gamma^{(\text{ew})}(t) = \Delta E_\gamma(t) - \underbrace{\frac{\epsilon_0 \epsilon_r A_{\text{SL}}(t) \phi^2}{2d}}_{E_e(t)}. \quad (3.5)$$

Equation (3.5) demonstrates why we reduce the electrical term to the capillary energy. Therefore, we write the global balance in the commonly used case with no external mechanical work, the energy budget reduces to:

$$\Delta(E_k + E_g + E_\gamma^{(\text{ew})}) = -E_d. \quad (3.6)$$

Figure 8 delineates the temporal evolution of the energy budget for two regimes: partial rebound (Fig. 8a) and deposition (Fig. 8b). The dynamics are predominantly governed by the interplay and conversion between kinetic energy (E_k), surface energy (E_γ), and viscous dissipation (E_d). In the case of partial rebound (Fig. 8a), the initial kinetic energy is rapidly depleted during the early spreading stage ($t^* < 0.4$), being primarily converted into surface energy to create a new liquid-gas interface and into energy dissipated through viscous effects. The surface energy peaks concomitantly with the maximum spreading diameter. Crucially, during the subsequent receding phase ($1.5 < t^* < 3.5$), a significant part of the stored surface energy is converted back into kinetic energy, driving the recoil of the lamella and the uplift of the central dome. However, the viscous dissipation E_d grows monotonically. This energy loss ultimately inhibits full recoil, leaving the droplet in a partially rebounded equilibrium state.

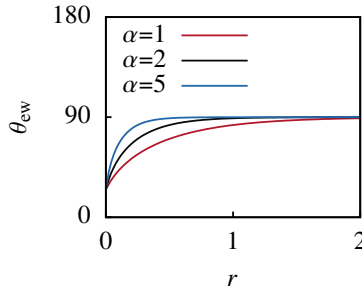


Figure 9: Radial variation of the substrate contact angle, θ_{ew} , induced by electrowetting.
The parameter α denotes different electric potential decay coefficients, from 1 to 5.

260 The final morphology is thus a direct consequence of the balance between the recoverable
261 surface energy and the energy lost to dissipation.

262 Conversely, the energy history for the deposition case (Fig. 8b) reveals a distinctly different
263 pathway. While the initial conversion from kinetic to surface energy is similar, the key
264 distinction lies in the retraction stage. Here, the dissipation rate is significantly higher, as
265 evidenced by the steeper slope of E_d , often due to stronger interactions within fluid. This
266 heightened dissipation effectively arrests the retraction stage. The energy available for recoil
267 is insufficient to overcome the combined effects of surface adhesion. The surface energy
268 keeps at a relatively high value with a significant reconversion into kinetic energy. Therefore,
269 the droplet will oscillate up and down repeatedly on the ground until all its kinetic energy
270 is exhausted, and settles into a stable, pancake-like deposited state. The energy budget
271 demonstrates that deposition arises once viscous dissipation exhausts the droplet's kinetic
272 energy and prevents the release of surface energy, effectively arresting the interface in a
273 minimum surface energystate.

274 The state of Complete rebound is noticed to exist widely in the range of We number less than
275 5. The bouncing mechanism is predicated on the persistence of an air film sustained at low
276 impact velocities. This sub-micrometre air cushion dissipates kinetic energy and reverses
277 the momentum of droplets. Consequently, the interposition of the air film prevents direct
278 contact between the droplet and substrate during low-velocity impact; thereby eliminating
279 wettability-dependent effects. As this mechanism has been extensively documented in prior
280 studies, it is not the primary focus of the present analysis.

281 3.2. Influence of Electric Potential Decay on Droplet Behavior

282 Incorporating a voltage decay coefficient into this model induces profound alterations in
283 droplet dynamics. Modifying the α -parameter in Equation 2.12 drastically perturbs the
284 interfacial voltage distribution. Consequently, the formerly uniform solid-liquid contact angle
285 is supplanted by a conical distribution-minimised centrally and maximised peripherally-
286 owing to voltage decay. Figure 9 illustrates the variation of the contact angle in the radial
287 direction under electrowetting conditions for different decay coefficients α . This funnel-
288 like contact angle profile enables the droplet to achieve a reduced contact angle upon initial
289 substrate contact. As the droplet spreads, the contact angle progressively increases. Compared
290 to uniform electrowetting surfaces, this configuration promotes enhanced droplet retraction
291 and rebound.

292 Figure 10 presents the temporal evolution of the droplet spreading radius under various
293 decay coefficients of electric potential, ranging from 0.01 to 5. Interrupted curves indicate
294 the occurrence of partial rebound, where the droplet detaches and emits secondary droplets.

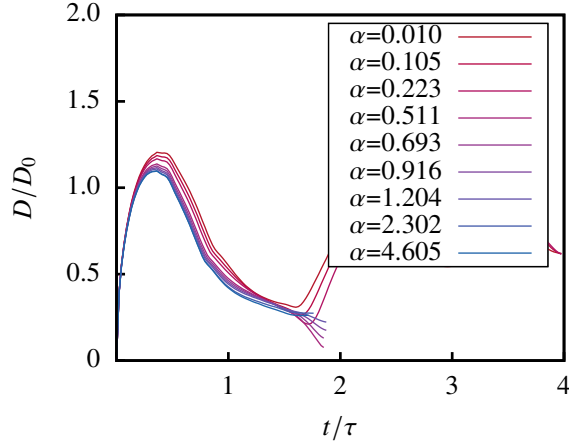


Figure 10: Temporal evolution of the normalized droplet spreading diameter versus normalized time for electric potential decay coefficients α ranging from 0.010 to 4.605.

295 It can be observed that for the decay coefficients of electric potential below 0.5, the droplet
 296 maintains a deposition state. However, as the decay coefficients of electric potential increases,
 297 the maximum spreading radius diminishes, and the droplet exhibits a heightened tendency
 298 towards partial rebound. As α approaches infinity, the droplet spreading behaviour converges
 299 towards that of impact onto a surface with a static 90° contact angle. Conversely, as α tends
 300 to zero, the spreading behaviour increasingly resembles the case of droplet impact under full
 301 electrowetting activation with a uniform contact angle θ_{ew} .

302 Subsequently, the energy evolution corresponding to 9 distinct values of the electrical
 303 dissipation coefficient α is plotted in figure 11. It is observed that as α increases, the
 304 energy distribution shifts from a low-dissipation regime, in which kinetic energy is fully
 305 dissipated, to a high-dissipation regime, where kinetic and surface energies undergo mutual
 306 conversion. Moreover, at the same final time, the proportion of surface energy increases
 307 with α . This trend is attributed to droplet partial rebound during retraction, which leads
 308 to the ejection of satellite droplets and a consequent significant increase in total surface
 309 area. Simultaneously, gravitational potential energy increases during retraction, ultimately
 310 converting into kinetic energy that facilitates partial rebound and detachment from the
 311 substrate. This behaviour contrasts with the deposition observed for lower α values (first row
 312 of the figure 11), wherein the droplet undergoes damped oscillations characterised by cyclic
 313 exchanges between gravitational potential and surface energy until the kinetic energy is fully
 314 dissipated.

315 To better characterise the evolution of kinetic energy, Figure 12 presents the kinetic energy
 316 as a function of time. The electrical dissipation coefficient α is shown to directly influence
 317 the kinetic energy profile. The kinetic energy reaches its minimum when the droplet attains
 318 its maximum spreading radius, at which point the kinetic energy is fully converted into
 319 surface energy, in line with the peak of the spreading radius curve. Subsequently, during
 320 rapid retraction, surface energy is converted back into kinetic energy, yielding the first peak
 321 in kinetic energy.

322 It is evident that increasing α markedly advances the time at which this first kinetic energy
 323 peak occurs. This is because the retraction phase is dominated by regions of high effective
 324 contact angle (approaching the 90° retraction behaviour), which generally promotes higher
 325 kinetic energy recovery. In the later stages of retraction, the reduction in contact angle has
 326 limited influence on kinetic energy (serving mainly to delay the second kinetic energy peak

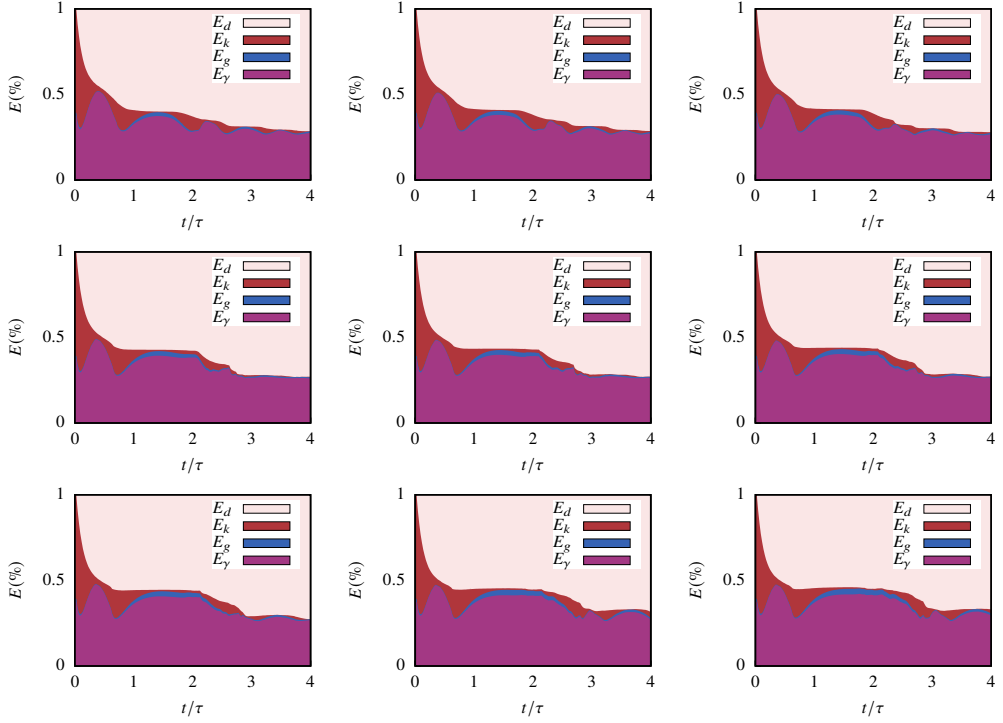


Figure 11: Temporal evolution of energy conversion during droplet impact on the substrate. From left to right, the panels correspond to increasing values of the electric potential decay coefficients α (from 0.010 to 4.605), identical to those in Figure 10. The abscissa indicates the dimensionless time, and the ordinate shows the partition among kinetic, surface, gravitational energies and dissipation.

327 during rebound), meaning that higher values of α typically result in greater kinetic energy
328 available for rebound.

329 At low α , the droplet cannot overcome the wetting influence of the substrate in the mid
330 to late stages of retraction. The droplet undergoes oscillations during which kinetic energy
331 is progressively dissipated, ultimately leading to deposition. In contrast, at high α , the first
332 kinetic energy peak attained during retraction is sufficiently large to overcome substrate
333 adhesion, resulting in partial rebound.

334 Through temporal integration of the energy energy over time on the wetted surface, the
335 electrical work expenditure W_{ew} effectively acting on the wetting behaviour of the substrate
336 is obtained, shown in figure 13. This smoothed profile serves as a measure of the fraction of
337 electrical energy actually consumed in altering the contact angle. It is shown that for lower
338 values of the electrical dissipation coefficient α , a greater proportion of electrical energy is
339 directly utilised to modify the contact angle during droplet spreading. This arises because
340 the evolution of wetting energy does not follow a simple linear trend, but rather evolves
341 through three distinct phases, owing to the funnel-like distribution of the substrate contact
342 angle during both spreading and retraction. Furthermore, this component of energy increases
343 most rapidly during the spreading stage, then enters a plateau region in the early retraction
344 phase, and continues to increase at a reduced rate in the later retraction stage. Only once the
345 droplet has stabilised on the substrate does W_{ew} attain a steady value.

346 A particularly intriguing outcome arises when electrode geometry and placement are tai-
347 lored to exploit potential dissipation, thereby enabling precise control of droplet morphology.

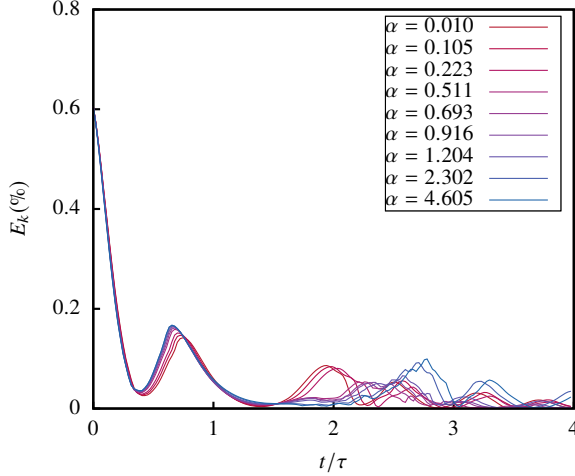


Figure 12: Evolution of the kinetic energy fraction with dimensionless time for different electric potential dissipation coefficients α during the process of droplet impact on the substrate. The horizontal axis represents dimensionless time, and the vertical axis represents the distribution of the kinetic energies.

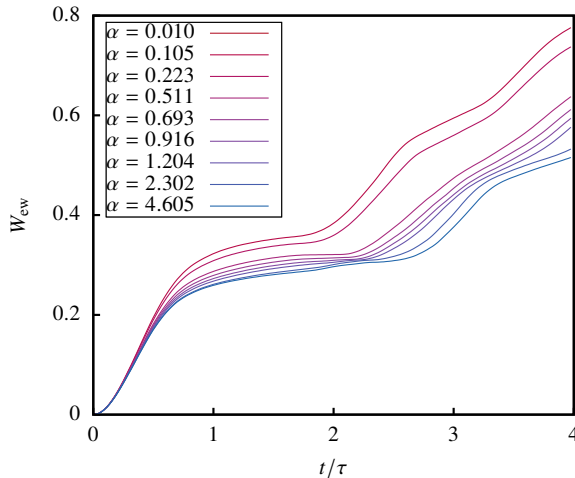


Figure 13: Evolution of electrical work expenditure W_{ew} effectively acting on the wetting of the substrate with dimensionless time for different electric potential dissipation coefficients α during the process of droplet impact on the substrate. The horizontal axis represents dimensionless time, and the vertical axis represents the distribution of the kinetic energies.

348 At $We = 100$ and an applied potential of 350 V, dissipation-driven modulation permits the
 349 formation of a ring-shaped droplet with remarkable ease—an outcome otherwise difficult to
 350 achieve by merely altering substrate chemistry. This effect relies on a highly resistive annular
 351 electrode positioned at the droplet diameter, where the potential field is prescribed as

$$352 \quad \phi(r, t) = \phi_0 \cos(2\pi f t) \cdot e^{-\alpha(r-r_0)^n}. \quad (3.7)$$

353 In this formulation, $\alpha \gg 1$ quantifies the coefficient of electric potential decay, $n = 30$

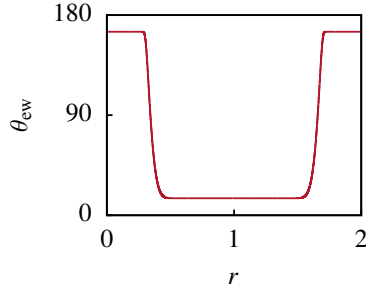


Figure 14: Radial variation of the electrowetting-induced substrate contact angle θ_{ew} for an annular electrode with the coefficient of electric potential decay taken into account.

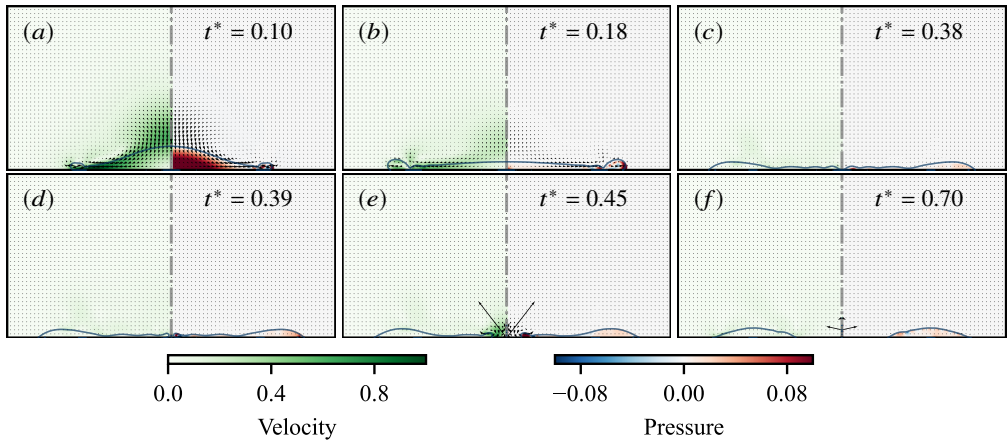


Figure 15: The formation process of ring-shaped droplets. The left snapshots show the magnitude of the velocity field normalized by the initial impact velocity, and the left snapshots show the dimensionless pressure. The black arrow is the velocity vector of flow. The blue line represents the interface between the droplet and the surrounding gas.

354 controls the width of the annular field, and $r_0 = D_0$ fixes its radial location. As demonstrated
 355 in Figure 14, the corresponding distribution of contact angle along the radial direction mimics
 356 a square-wave profile, yet remains governed by the electric potential decay functional form.
 357 Such electrode-enabled control offers a powerful and effective strategy for manipulating
 358 droplet dynamics beyond conventional surface treatments.

359 As for the formation of the annular droplet, the mechanism is similar to that induced
 360 by a wettability discontinuity. The droplet first undergoes complete spreading and wetting.
 361 Subsequent retraction towards the centre generates intense capillary waves, which converge
 362 at the droplet's axis. These waves induce pronounced vertical oscillations on the upper
 363 surface of the droplet. As the amplitude of these oscillations increases, the rising liquid
 364 interface interacts with an entrapped gas cavity, ultimately triggering the formation of a
 365 central through-hole. The droplet then retracts radially outward from this hole, eventually
 366 stabilising into a toroidal structure. A detailed dynamical description and energy analysis of
 367 this process has been provided in our previous publication and is therefore not repeated here.

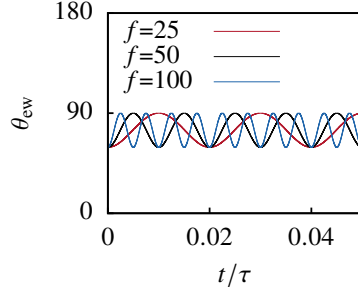


Figure 16: Comparison of drop spreading radius during impact process obtained from simulations at $We = 20$.

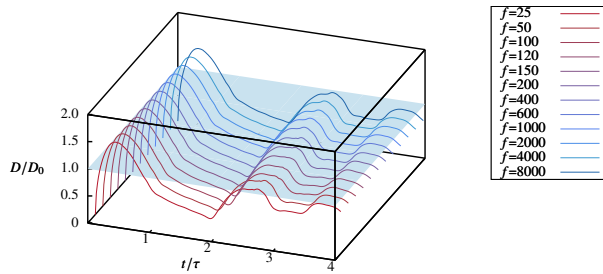


Figure 17: Comparison of drop spreading radius during impact process obtained from simulations at $We = 20$.

368

3.3. Frequency-Dependent Response of Electrowetting-Induced Motion

369 The frequency of electrowetting significantly influences the wetting radius and oscillation
 370 amplitude of a sessile droplet. A sessile droplet subjected to an alternating electrowetting
 371 signal exhibits vertical oscillations. However, the manner in which frequency variation affects
 372 droplet spreading and retraction during impact remains an open question. To investigate this,
 373 we varied the driving frequency f from 25 to 8000 Hz. This frequency sweep induces a
 374 cyclic variation of the contact angle at the wall, which decreases from 90° to a minimum
 375 value (approximately 60°) and then returns to 90° , following a cosine functional form.
 376 Such variation in contact angle alters the force balance associated with wetting dynamics
 377 throughout the droplet's motion. Figure 18 illustrates the temporal evolution of the contact
 378 angle at the substrate for different driving frequencies.

379 At the moment the droplet is released, the voltage is activated on the substrate, inducing
 380 a time-dependent contact angle variation governed by the Young-Lippmann equation. Since
 381 the contact angle remains consistently below 90° , no thin air film forms between the droplet
 382 and the substrate upon contact. Consequently, the spreading and retraction dynamics are
 383 entirely governed by the evolving substrate contact angle. The Weber number of the droplet
 384 impact was fixed at 35 and the voltage amplitude at 180 V to ensure that the droplet's motion
 385 remained within the deposition regime. Throughout the deposition process, the droplet
 386 initially impacts the substrate, then gradually equilibrates under the combined influence of
 387 inertial and capillary forces, and ultimately stabilises on the surface. Even with increasing
 388 voltage frequency, the droplet continues to exhibit the characteristic dynamic stages of
 389 spreading, retraction, and rebounding during the process of deposition.

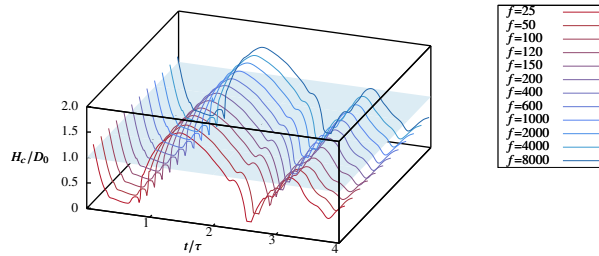


Figure 18: Comparison of drop spreading radius during impact process obtained from simulations at $We = 20$.

390 4. Conclusion

391 **Funding.** This research was supported in part by the National Natural Science Foundation of China (No.
392 11972170).

393 **Declaration of interests.** The authors report no conflict of interest.

394 **Author ORCIDs.** Authors may include the ORCID identifiers as follows. Ziqiang Ma, <https://orcid.org/0000-0003-3608-0199>; Xinping Zhou, <https://orcid.org/0000-0001-6340-5273>

REFERENCES

- 396 AFKHAMI, S., BUONGIORNO, J., GUION, A., POPINET, S., SAADE, Y., SCARDOVELLI, R. & ZALESKI, S. 2018
397 Transition in a numerical model of contact line dynamics and forced dewetting. *J. Comput. Phys.*
398 **374**, 1061–1093.
- 399 AFKHAMI, S., ZALESKI, S. & BUSSMANN, M. 2009 A mesh-dependent model for applying dynamic contact
400 angles to VOF simulations. *J. Comput. Phys.* **228** (15), 5370–5389.
- 401 CHENG, Y., WANG, F., XU, J., LIU, D. & SUI, Y. 2018 Numerical investigation of droplet spreading and heat
402 transfer on hot substrates. *International Journal of Heat and Mass Transfer* **121**, 402–411.
- 403 DUVIVIER, D., BLAKE, T.D. & DE CONINCK, J. 2013 Toward a predictive theory of wetting dynamics.
Langmuir **29** (32), 10132–10140.
- 405 JIAN, Z., JOSSERAND, C., POPINET, S., RAY, P. & ZALESKI, S. 2018 Two mechanisms of droplet splashing on
406 a solid substrate. *Journal of Fluid Mechanics* **835**, 1065–1086.
- 407 KOROBKIN, A.A., ELLIS, A.S. & SMITH, F.T. 2008 Trapping of air in impact between a body and shallow
408 water. *J. Fluid Mech.* **611**, 365–394.
- 409 KUMAR, A. & PATHAK, M. 2024 Droplet impact characteristics on hydrophobic surfaces with partial
410 electrowetting effects. *Physics of Fluids* **36** (9), 092126.
- 411 LI, E.Q. & THORODDSEN, S.T. 2015 Time-resolved imaging of a compressible air disc under a drop impacting
412 on a solid surface. *J. Fluid Mech.* **780**, 636–648.
- 413 MANDRE, S., MANI, M. & BRENNER, M.P. 2009 Precursors to Splashing of Liquid Droplets on a Solid
414 Surface. *Phys. Rev. Lett.* **102** (13), 134502.
- 415 McHALE, G., BROWN, C.V., NEWTON, M.I., WELLS, G.G. & SAMPARA, N. 2011 Dielectrowetting driven
416 spreading of droplets. *Physical Review Letters* **107** (18), 186101.
- 417 POPINET, S. 2003 Gerris: a tree-based adaptive solver for the incompressible euler equations in complex
418 geometries. *J. Comput. Phys.* **190** (2), 572–600.
- 419 POPINET, S. 2009 An accurate adaptive solver for surface-tension-driven interfacial flows. *J. Comput. Phys.*
420 **228** (16), 5838–5866.
- 421 SMITH, F.T., LI, L. & WU, G.X. 2003 Air cushioning with a lubrication/inviscid balance. *J. Fluid Mech.* **482**,
422 291–318.
- 423 ŠIKALO, V., MARENGO, M., TROPEA, C. & GANIĆ, E.N. 2002 Analysis of impact of droplets on horizontal
424 surfaces. *Experimental Thermal and Fluid Science* **25** (7), 503–510.